Practical Data Acquisition Strategy for Time-lapse Experiments Using Crosshole GPR and Full-Waveform Inversion

Johanna Keskinen (1,3), Majken C. Looms (1), Anja Klotzsche (2), and Lars Nielsen (1)

(1) Department of Geosciences and Natural Resource Management, University of Copenhagen, Øster Voldgade 10, 1350, Copenhagen, Denmark

(2) Agrosphere (IBG-3), Institute of Bio- and Geosciences, Forschungszentrum Jülich GmbH, 52428 Jülich, Germany

(3) Geological Survey of Finland, Vuorimiehentie 5, 02151 Espoo, Finland

Abstract

Crosshole ground penetrating radar (GPR) methods are increasingly used in time-lapse studies of flow in the uppermost near subsurface with important implications for our understanding of e.g., water infiltration in the unsaturated zone, and fluid flow in the saturated zone. A particular challenge in such time-lapse crosshole studies is the trade-off between collecting sufficient data to be able to resolve how a tracer moves, and, minimizing the data acquisition time such that the data approximates a static state. We test how dense recording geometries are needed for resolving a gas bubble injected in a highly heterogeneous chalk reservoir analogue using a full-waveform inversion (FWI) approach for modelling the crosshole GPR data. We show that even relatively sparse geometries provide sufficient resolution of the permittivity contrast caused by the gas bubble, provided that the detailed background permittivity structure is known from prior (before gas injection) FWI analysis of densely recorded high-resolution data. The conductivity contrast caused by the gas is more challenging to recover and the resolution suffers to a higher degree when reducing the survey geometry or at higher noise levels. As long as the permittivity change during the time-lapse experiment is the main target, a significant reduction in acquisition time is therefore possible as compared to the time needed to record the background permittivity structure. This reduced acquisition time has important practical implications for time-lapse

experiments under realistic conditions. Our results are based on synthetic analysis based on a realistic subsurface scenario closely linked to characterization of heterogeneous chalk reservoirs. However, our findings also have important implications for planning of future time-lapse studies in other settings.

1. Introduction

Time-lapse experiments using crosshole ground-penetrating radar (GPR) tomography are efficient in characterizing changes in water saturation in the near subsurface (see update paper by Klotzsche et al., 2018). Knowledge obtained from time-lapse experiments is important, for instance when characterizing recharging of aquifers, flow in reservoir rocks, as well as contaminant transport in the subsurface (e.g., Hubbard et al., 1997; Binley et al., 2001; Day-Lewis et al., 2003; Looms et al., 2008; Haarder et al., 2012; Lassen et al., 2015).

A tracer fluid or gas is typically injected into the formation and its flow across the studied interval is monitored by collecting GPR data at selected time intervals. The radar wave velocity is mainly controlled by the relative permittivity of the subsurface, and is highly sensitive to the moisture content of the sampled volume because of the substantial difference between the relative permittivity $\varepsilon_r = 1$ of air (gas) and water $\varepsilon_r \approx 80$ (Davis and Annan, 1989). Further, variations in electrical conductivity caused by the applied tracer may result in radar wave amplitude changes that are strong enough to affect the results obtained from application of FWI (Meles et al., 2010; Klotzsche et al., 2019). Interpretation of time-lapse data has largely been carried out applying ray-based inversion methods (e.g., Binley et al., 2001; Looms et al., 2008). Here, differences in the resulting subsurface tomograms obtained for different times after fluid/gas injection are interpreted to show the tracer movement and extension.

The applied tracer is typically designed to create a strong contrast to the background media. Strong anomalies of small size are difficult to handle for ray-based inversion methods because of the inherent limitations linked to such approaches. The resolution of the subsurface models is improved by using full-waveform inversion (FWI). Several case studies have applied the FWI algorithms developed by Ernst et al. (2007a) and Meles et al. (2010), and demonstrated that FWI resolves small-scale structures and higher resolution images than ray-based inversion methods (e.g., Ernst et al. 2007b; Klotzsche et al., 2013; Gueting et al., 2017 and Keskinen et al., 2017). Furthermore, Klotzsche et al. (2013) were able to correlate a zone of higher permittivity with zones of preferential flow within a gravel aquifer indicating the possibility to detect preferential flow paths of gas and water in different environments.

A key aspect in time-lapse GPR experiments is the selected data acquisition strategy. When collecting data for crosshole tomography, the subsurface is typically sampled using the so-called ‘multiple offset gather’ (MOG) acquisition technique presented e.g., in Binley et al. (2001). With this measurement geometry, a transmitter antenna is kept in fixed positions in one borehole while a receiver antenna is lowered in discrete steps in the other borehole illuminating the section between the boreholes at different angles. Such an acquisition strategy allows for resolving the subsurface variations vertically and to some extent laterally. If mainly vertical changes (horizontal layering) in the studied section are relevant, the subsurface can also be sampled efficiently using so-called zero-offset profiling (ZOP), where transmitter and receiver antennae are lowered in parallel down the boreholes in discrete steps (see e.g., Binley et al., 2001). In both cases the collected datasets have to be dense enough to provide reliable results for the target of the investigation. Nevertheless, time consuming data collection with many transmitter-receiver positions may be problematic due to possible significant fluid/gas movement during the acquisition time interval. For example, Lassen et al. (2015) observed that gaseous $C0_2$ migrated laterally approximately 2 m away from the injection point during only two hours.

The resolution study conducted by Oberröhrmann et al. (2013) focused on optimizing transmitter and receiver spacing to obtain adequate ray coverage for reliable FWI results, while reducing computation time. They used for example the MOG data acquisition with 0.5 m transmitter spacing and 0.1 m receiver spacing, and, repeated the measurements after changing the transmitter and receiver boreholes using a semi-reciprocal setup. This approach resulted in approximately 4.5 hours of data acquisition time. Also, Keskinen et al. (2017), Ernst et al. (2007b), and Yang et al. (2013) choose a sampling strategy to ensure dense data coverage for FWI by performing either two-sided or one-sided dense measurements (higher computational costs). Coarser transmitter and receiver spacing are applied in the experiments of Ernst et al. (2007b) and Klotzsche et al. (2014). Their results suggest that sufficient ray coverage for reliable FWI results may also be obtained with a sparser dataset and hence shorter acquisition times.

The tracer migration in the subsurface sets a strict time limit on crosshole GPR data collection. Therefore, we study the trade-off between the acquisition time and the resolution of the models obtained from FWI of crosshole GPR data. Specifically, we apply different acquisition strategies for resolving models that illustrate a time-lapse experiment, where gas is injected into a strongly heterogeneous water-saturated medium to form a small, but strong/distinct anomaly to the surroundings. For this purpose, we use realistic subsurface relative permittivity ε_r and electrical conductivity σ distributions obtained from the FWI crosshole GPR study by Keskinen et al. (2017) and apply FWI to investigate how each of the selected data acquisition geometries perform in resolving the location, size and magnitude of the anomaly. Thus, in contrast to earlier synthetic resolution studies, we base our investigations on a concrete case, where highly contrasting chalk deposits are investigated. Study of this chalk sequence is considered essential for improved reservoir characterization of onshore groundwater reservoirs in Denmark and offshore hydrocarbon reservoirs in the North Sea. Moreover, since the studied sequence has been mapped with high resolution crosshole GPR data using FWI analysis (Keskinen et al., 2017), we only need to resolve variations from the already established high-resolution image in our synthetic time-lapse experiments. Trade-offs between realistic acquisition times, resolution of the tracer anomaly, the effect of noise, and possible tracer movement during data acquisition are discussed.

2. Designing the synthetic experiment

2.1 Acquisition geometries

Former FWI studies conducted with experimental crosshole GPR data used different choices for the data acquisition geometry and the resulting data coverage. For example, the experiments by Ernst et al. (2007b) and Yang et al. (2013) used transmitter spacing from 0.4 m to 0.5 m, while the receiver spacing varied from 0.05 m to 0.5 m, respectively. They used the MOG data acquisition technique and kept the transmitter in one borehole, while the receiver was kept in the other borehole. Thus, for those experiments the dataset is one-sided. If the transmitter or the receiver spacing is large, the ray coverage may be too sparse and may lead to poor FWI results, in particular close to the model edges and boreholes. Oberrörhmann et al. (2013) compared three different acquisition geometries and their impact on the resolution of the obtained subsurface models. The investigated datasets of that study consisted of a one-sided sparse geometry with 0.5 m transmitter and 0.1 m receiver spacing, and a one-sided dense geometry with 0.1 m transmitter and receiver spacing. The third dataset investigated by Oberrörhmann et al. (2013) was a two-sided setup, which was composed of two subsets with transmitters at every 0.5 m and receivers at every 0.1 m. The first subset of the two-sided data was recorded by keeping a transmitter in the first borehole, while a receiver is kept in the other borehole. For the second subset, the transmitter and receiver locations were interchanged (semi-reciprocal). The semi-reciprocal setup was introduced by Klotzsche et al. (2010) to minimize the acquisitions time and the computational cost for the FWI. Oberrörhmann et al. (2013) conclude that the two-sided setup results in acceptable FWI results, while reducing both computing time and acquisition time by reducing the number of measurement points. While the dense one-sided dataset takes approximately 9 hours to collect, the two-sided dataset is collected in only 4.5 hours. Klotzsche et al. (2014) used 100 MHz antennae systems and even sparser sampling with a transmitter spacing of 1 m and a receiver spacing of 0.25 m. As this dataset was two-sided, the ray coverage close to the boreholes was sufficient for reliable FWI results in their case.

We choose to investigate two-sided crosshole datasets and compare seven different survey geometries (see Fig. 1). The dense two-sided MOG acquisition geometry from Keskinen et al. (2017) is used as the reference geometry (see Fig. 1A) and is also the geometry used to achieve the background permittivity distribution. Thus, the reference recording geometry used here consists of 40 transmitter positions, one at every 0.5 m down a 15 m deep borehole. For each transmitter gather, we have 156 receiver positions, one at every 0.0625 m, resulting in a total of 6240 recorded traces. For the 100 MHz PulseEKKO GPR system (Sensors & Software, ON, Canada) used by Keskinen et al. (2017), the first side (20 transmitter gathers) of such a dataset requires approximately 4.3 hours of data collection, assuming that the time delay between each trace is 3 seconds, and that the additional time needed between subsequent transmitter gathers is 5 minutes. Note that also the choice of time window, time sampling and stacking of the traces is affecting the acquisition time, which are assumed to be constant for this study.

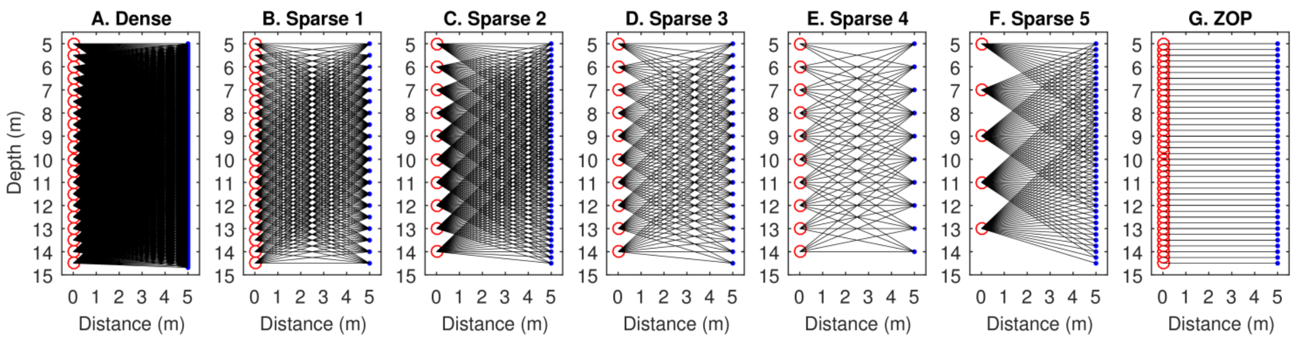

Figure 1: Data coverage for the first half of each dataset transmitter positions are indicated with red circles and receiver positions with blue dots. Table 1 shows the data acquisition parameters for each of the survey geometry.

Other, sparser, recording geometries are designed and tested. The sparse two-sided MOG survey geometries; Sparse 1-5 (Fig. 1B-F), are different subsets of the dense geometry. They are designed so that only the receiver spacing is increased (Sparse 1) or that both the transmitter and the receiver spacing are increased (Sparse 2-5). In addition, we test one ZOP strategy with 25 cm transmitter and receiver spacing (Fig. 1G). The data collection routine in the field requires at least the following steps:

1. Collect starting calibration data (time-zero correction) for the first half of the entire data.
2. Record the first side of the entire MOG dataset or record the first ZOP data (transmitter in borehole 1, receiver in borehole 2).
3. Collect calibration data.
4. Carry out required tasks to record the second half of the dataset (e.g., move the equipment, change batteries).
5. Collect starting calibration data for the second half of the entire dataset.
6. Record the second half of the entire MOG dataset or record the second ZOP data (transmitter in borehole 2, receiver in borehole 1).
7. Collect final calibration data.

We assume that the time needed for the starting calibration (for correcting the time zero of the data), the final calibration and the time needed for interchanging the transmitter and receiver boreholes is the same for all survey geometries. Also, both MOG and ZOP data are collected as two-sided datasets. This is done to ensure that all data analysis is conducted exactly the same manner for all of the tested survey geometries. For the ZOP survey a one-sided dataset would, in principle, provide the same information as the two-sided. Table 1 compares the acquisition times for the first half of each acquisition setup. Table 1 also shows the survey parameters for all recording geometries.

	Dense	*Sparse 1*	*Sparse 2*	*Sparse 3*	*Sparse 4*	*Sparse 5*	*ZOP*
Transmitter spacing (m)	0.5	0.5	1	1	1	2	0.25
Receiver spacing (m)	0.0625	0.5	0.25	0.5	1	0.25	0.25
Number of transmitter positions	40	40	20	20	20	10	78
Number of receiver positions	312	40	78	40	20	78	78
Number of collected traces	6240	800	780	400	200	375	78
Number of traces used in FWI	4078	521	510	260	128	253	78
Acquisition time per transmitter gather (mins)	7.8	1	2	1	0.5	2	-
Estimated acquisition time per the first half of the dataset (mins)	256	120	70	60	55	35	7

Table 1: Survey geometries shown together with the estimated data acquisition times for an individual transmitter gather (MOG and ZOP strategies) as well as for half a dataset, respectively. Number of recorded traces differs from the number of traces used in the FWI.

For ray-paths with high angles an increasing apparent-velocity can be observed, and to avoid artefacts in the tomographic inversion the field data has to be reduced (Peterson, 2001; Irving and Knight, 2005). Therefore, transmitter-receiver pairs that have an angle higher than 40 degrees above the horizontal are removed from the datasets used in FWI. Table 1 shows the number of traces used in FWI for each tested survey geometry and Figure 1 illustrates the data coverage of these recording geometries.

2.2 True Subsurface Models and Synthetic GPR Data

2.2.1 The background models

As mentioned above, Keskinen et al. (2017) applied FWI on GPR data collected in a chalk quarry to map heterogeneity of the rocks and estimate a high-resolution porosity model in the fully water-saturated part of the studied section. We use the final subsurface permittivity ε_r, conductivity σ, and bulk porosity φ distributions from their study as reference models representing the situation before a gas bubble is introduced into the subsurface. Moreover, for simplicity the mean groundwater conductivity of 88.1 mS/m from their measurements is chosen for this study.

2.2.2 Influence of a gas bubble

Tracer experiments, e.g., by Hubbard et al. (1997), Tomlinson et al. (2003), Cahill et al. (2013), and Lassen et al. (2015), show that a tracer substance can create strong local anomalies with gas saturation from 30% up to 65%. Therefore, in our synthetic test modelling the true subsurface models represents a setting where gas has partially replaced a small volume of pore water from the reference ε_r and σ models. The water saturation in the gas bubble is 70% and the electrical properties of the gas are assumed the same as for air. Mount and Comas (2014) compared different methods to estimate porosity in a limestone sample and concluded that complex refractive index model (CRIM) (e.g., Lesmes and Friedman, 2005) performs well in estimating bulk porosities from GPR measurements. Also, Keskinen et al. (2017) assumed that the dielectric properties of chalk do not significantly differ from those of limestone. In this study, the influence of the gas on the bulk permittivity ε_b is therefore calculated using the previously estimated bulk porosities φ and CRIM for partially saturated media (Lesmes and Friedman, 2005):

$$\sqrt{\varepsilon_b} = S\phi\sqrt{\varepsilon_w} + \phi(1-S)\sqrt{\varepsilon_a} + (1-\phi)\sqrt{\varepsilon_m}. \quad (1)$$

The rock matrix is considered to be pure calcite and the permittivity values for water, air and calcite are $\varepsilon_w = 80$, $\varepsilon_a = 1$ and $\varepsilon_m = 8$, respectively (Davis and Annan, 1989; Lebron et al. 2004). Water saturation in fraction is indicated with S.

A first-order estimate of the influence of the gas bubble on the bulk conductivity σ_b is estimated using Archie's law (e.g., Lesmes and Friedman, 2005) for partially saturated media, and the groundwater conductivity (σ_w = 88.1 mS/m, Keskinen et al., 2017) and the previously obtained bulk porosity model φ are assumed to be related as follows:

$$\sigma_b = \sigma_w \phi^m S^d, \quad (2)$$

where m is the cementation exponent and d is the saturation index. Witthüser et al. (2000) collected chalk samples close to the study area of Keskinen et al. (2017) and estimated the cementation exponent m = 2.2 for these samples. We use the same value for this synthetic study.

The saturation index *d* is usually larger than the cementation factor *m* because the conducting paths become more tortuous with decreasing saturation (Lesmes and Friedman, 2005). For simplicity, we choose a saturation index *d* = 2.2 in our study, as this also gave reliable results in Keskinen et al. (2017).

2.2.3 Calculation of synthetic crosshole GPR data

Synthetic noise-free GPR data for each acquisition setup are obtained using the 2D forward modeling algorithm by Meles et al. (2010), which is based on finite-difference solutions of Maxwell's equations in the time-domain. The final FWI results of the subsurface ε_r, σ, and the effective source wavelet of Keskinen et al. (2017) are used to derive the synthetic data. The source wavelet has a center frequency of 27 MHz. The resulting GPR datasets (measured data) have a frequency spectrum comparable to experimental crosshole GPR data collected from water-saturated chalk as the center frequency of the recorded signals varies between less than 30 to ~70 MHz, depending on the depth of the studied interval (see Keskinen et al. (2017) for more details).The gas bubble was added at a depth of approximately 11 m. Noisy datasets are obtained by adding random noise on the modeled noise-free GPR data. We assume that the noise is Gaussian with a mean amplitude $\overline{A}$=0 and standard deviation *std* = 0.51×10^{-6} for a low noise scenario, *std* = 1.02×10^{-6} for an intermediate noise scenario, and *std* of 1.53×10^{-6} for a high noise scenario (Figure 2). The level of noise in the high-noise scenario is determined by choosing the remaining root-mean-square-error *rms*=1.53×10^{-6} from the final FWI results in Keskinen et al. (2017). The noise estimated this way is rather high compared to the observations from the experimental data in their study, see Figure 2C. Therefore, it is reasonable to test the other two scenarios as well. The intermediate and low noise levels are 1/3 and 2/3 of this value, respectively (Figures 2A and 2B).

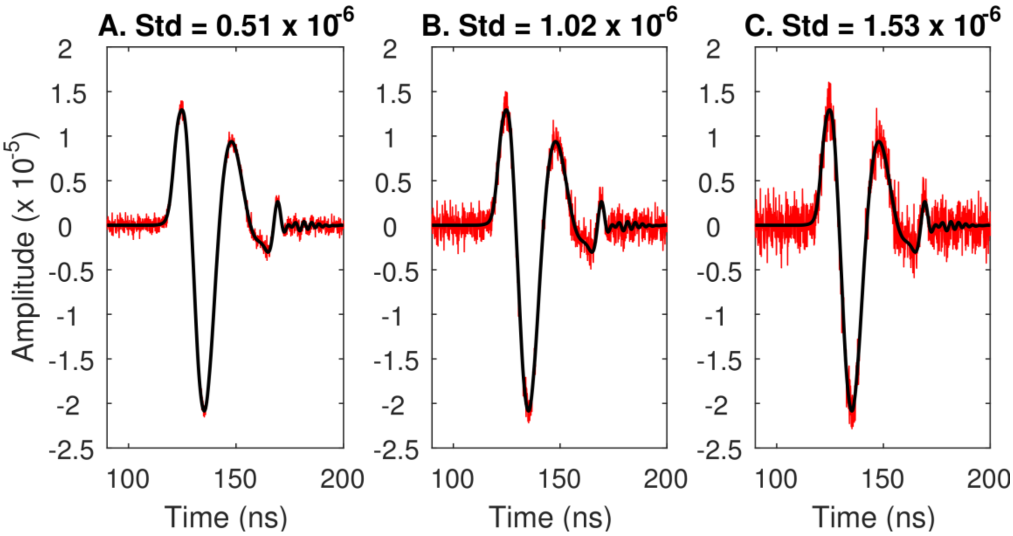

Figure 2: (A) Low, (B) intermediate, and (C) high noise added on the synthetic data (red). The noise is random Gaussian noise with a standard deviation *std* of, $0.51\cdot10^{-6}$, $1.02\cdot10^{-6}$, and $1.53\cdot10^{-6}$, respectively. The black trace represents the noise free trace.

2.3 Full-waveform inversion of crosshole GPR

FWI method is based on a conjugate-gradient type inversion scheme that simultaneously retrieves the subsurface ε and σ distributions (more detail in Meles et al., 2010). One of the main challenges in applying this method on field data is finding suitable starting models for ε and σ, as well as finding a representative effective source wavelet to describe the interaction between the formation and the emitted electromagnetic wave (e.g., Klotzsche et al., 2019; Keskinen et al., 2017). In this synthetic study, we use the final effective source wavelet estimated by Keskinen et al. (2017) and assume that source wavelet is not changing during the injection. Therefore, differences in the FWI results arise from the survey geometries only and are not influenced by the source wavelet. The gas bubble changes the electrical properties of the subsurface in a small area, while most of the model remains the same. It is therefore reasonable to assume that the source wavelet estimated using a fully water-saturated model and a source wavelet estimated from the models with a gas bubble do not significantly differ from each other. Note that in realistic tracer experiments an effect on the effective source wavelet could be expected if changes in the borehole fillings are present (Klotzsche et al., 2019).

The FWI method of Meles et al. (2010) is solving the misfit function $C(\varepsilon,\sigma)$ between modeled $\boldsymbol{E}^{s}(\varepsilon,\sigma)$ and measured electrical $\boldsymbol{E}_{obs}^{s}(\varepsilon,\sigma)$:

$$C(\varepsilon,\sigma) = \frac{1}{2}\sum_{s}\sum_{d}\sum_{\tau}\left[\boldsymbol{E}^{s}(\varepsilon,\sigma) - \boldsymbol{E}_{obs}^{s}(\varepsilon,\sigma)\right]_{d,\tau}^{T} \cdot \delta(\boldsymbol{x} - \boldsymbol{x}_{d}, t - \tau)\left[\boldsymbol{E}^{s}(\varepsilon,\sigma) - \boldsymbol{E}_{obs}^{s}(\varepsilon,\sigma)\right]_{d,\tau}. \tag{3}$$

The sum is calculated over sources *s*, receivers *d* and observation times τ; δ is the Dirac's delta function, *t* the time, **x** the location and $\mathbf{x}_{d}$ the receiver position. Vectors are denoted with bold letters. The electrical fields are modeled by solving Maxwell's equations with finite-difference approach in time-domain and consider the vectorial behavior of the fields. The FWI algorithm of Meles et al. (2010) finds the minimum of the misfit function $C(\varepsilon,\sigma)$ by applying a gradient based iterative least-squares method. At each iteration (step *k*), first synthetic electrical fields $\boldsymbol{E}^{s}(\varepsilon,\sigma)$ are calculated using the current subsurface models (ε_k and σ_k). Second, the subsurface model update directions ∇C_{ε} and ∇C_{σ} are estimated. Third, two step lengths ζ_{ε} and ζ_{σ} are calculated to determine how much the subsurface ε_k and σ_k models need to be updated for the next iteration (step *k*+1) to minimize the cost function. The next iteration (*k*+1) is carried out the same way as above, but with the new updated subsurface models (ε_{k+1} and σ_{k+1}). The process continues until the FWI has converged, the root-mean-square-error *rms* between to subsequent iterations is changing less than 0.5%, and is in total reduced by minimum 50% compared to the starting models.

The FWI method requires suitable starting models ε_0 and σ_0 that provide synthetic data within half a wavelength of the measured data to able to perform the first iteration step (Meles et al., 2010). We used as starting models the final permittivity and conductivity models of Keskinen et al. (2017), which represent the fully water-saturated subsurface before the tracer gas is injected into the subsurface. The model area for the inversion is discretized into 12 cm by 12 cm cells (forward model 3 times finer), and we define a damping zone of 48 cm wide around the boreholes locations. In these zones, the model updates by the FWI are heavily dampened to avoid strong artefacts close to model edges. Outside the dampening zones, the FWI is allowed to freely update the subsurface models. Perturbation factors that are necessary for the step length calculations need to be define and optimized in the beginning of the FWI. These factors influence the magnitude of the allowed subsurface model updates. In this study, these perturbation factors are optimized so that the obtained results have the smallest *rms* while the anomaly shape and magnitude induced by the gas bubble are well-constrained.

The final FWI results is decided when following criteria are fulfilled: *rms* curve converges, the *rms* between modeled and measured data changes less than 0.5% between subsequent iterations, the total *rms* is decreased by at least 50% from the starting model, a good fit between the measured and modeled data in the entire domain, and remaining permittivity and conductivity gradients have decreased close to zero value. The *rms* criterion is based on the observation that the final subsurface models remain practically unchanged during the following iterations even if the data used is noise-free. Setting a stricter *rms* criterion, for example 0.1%, does not bring any additional information on the final results. The *rms* criterion is applied both on the noise-free and noisy data. Therefore, the number of iterations needed to reach the convergence criterion is different for each presented test. The number of iterations needed for convergence decreases when the level of noise increases.

3. Results

3.1 Different acquisition setups

The true subsurface input ε_r and σ distributions including the gas bubble used for testing are shown in Figures 3A and 4A. The gas bubble permittivity in the true ε_r distribution is approximately 13 units lower than in the background distribution forming a strong and small low-permittivity target in high permittivity material (Fig. 3A, 3I). In the true σ distribution, the same target appears as an anomaly having approximately 10 mS/m lower conductivity than in the surrounding material (Fig. 4A, 4I). The resolved ε_r and σ images using the different acquisition strategies are shown in Figures 3B-3H and 4B-4H, respectively. The number of traces used in the FWI for each case is indicated in Table 1.

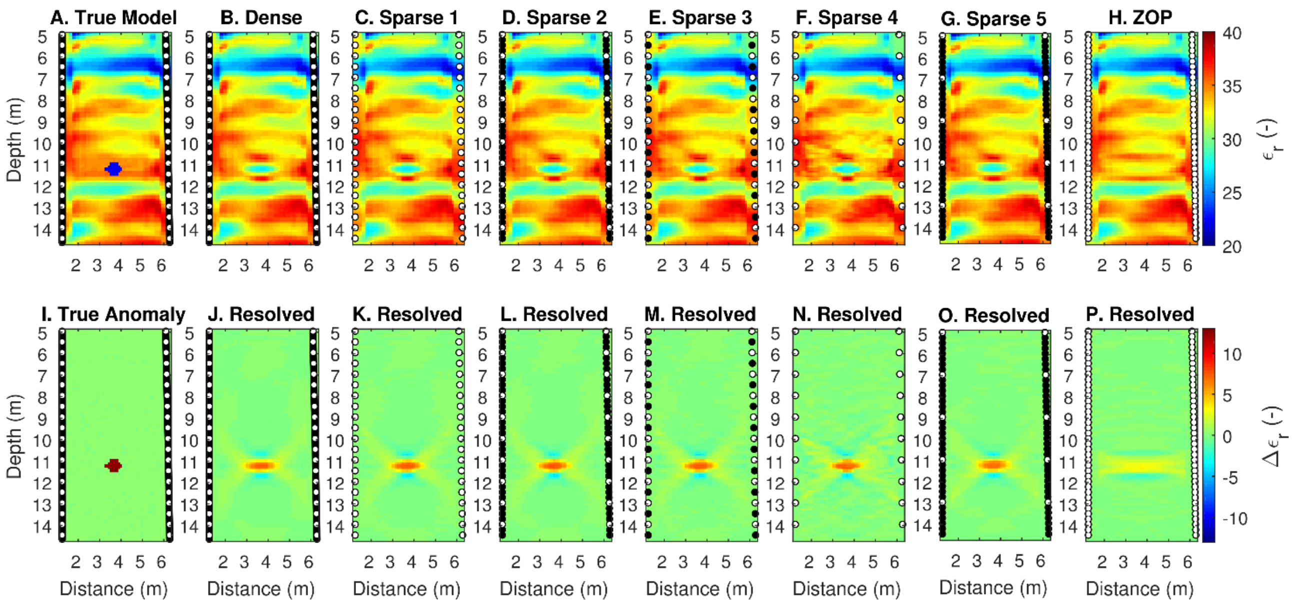

Figure 3: The true subsurface ε_r model (A) and the resolved ε_r models obtained from the different acquisition geometries (B-H). True anomaly magnitude (I) is obtained by subtracting the true subsurface ε_r model from the ε_r starting model. The resolved anomaly magnitudes (J-P) are estimated by subtracting the final ε_r model from the ε_r starting model. Transmitter and receiver positions are indicted with circles and crosses, respectively.

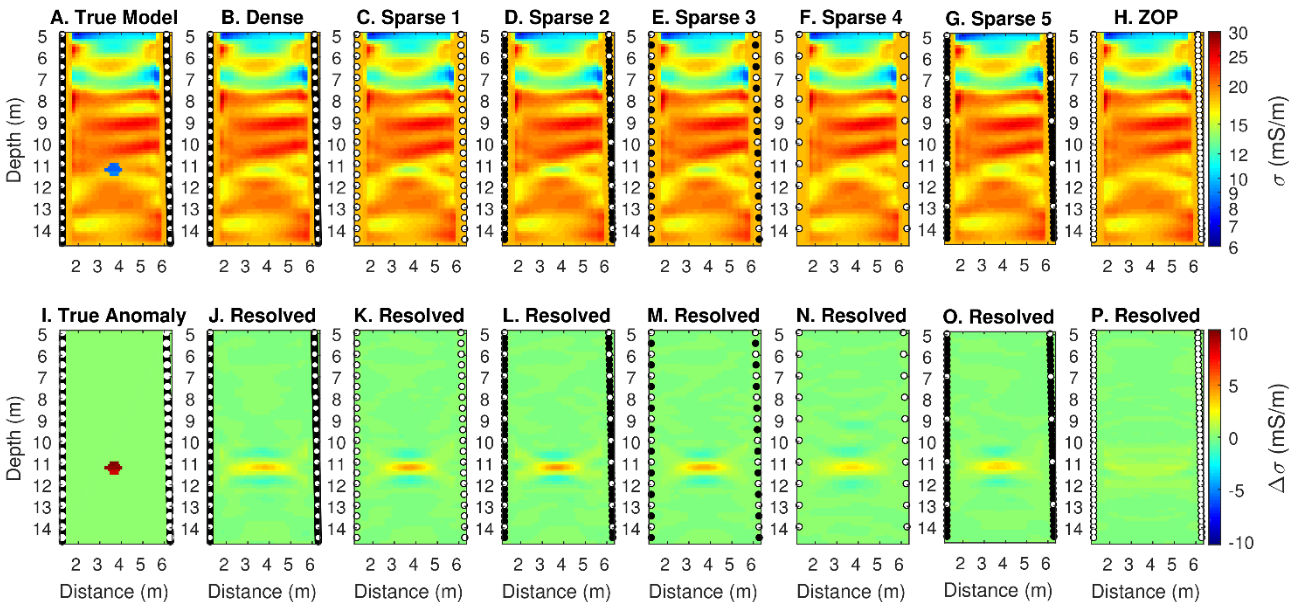

Figure 4: The true subsurface σ model (A) and the resolved σ models obtained from the different acquisition geometries (B-H). True anomaly magnitude (I) is obtained by subtracting the true

subsurface σ model from the σ starting model. The resolved anomaly magnitudes (J-P) are estimated by subtracting the final σ model from the σ starting model.

The resolved permittivity distributions show that all sparse setups using MOG data acquisition perform well in resolving the location and the shape of the gas bubble (Figs. 3C-3G, 3J-2O). However, Sparse Geometry 4 with 1 m transmitter and 1 m receiver spacing has some difficulties resolving the background distribution suggesting that the dataset is reduced too much (Fig. 3F). The models obtained from Sparse Geometries 1-5 have slightly higher permittivity directly above and below the gas bubble than in the model resolved using the dense reference geometry (Fig. 3B-3G, 3J-3O). The dense reference setup results in a slightly more horizontally elongated bubble than the sparse geometries. The recovered maximum anomaly magnitude for each acquisition setup is presented in Table 2. All MOG surveys estimated the magnitude of the permittivity anomaly in a similar manner. In the very center of the gas bubble, the resolved anomaly magnitude is 53-60% of the true magnitude (Figs. 3I-3O). The maximum value represents one cell in the bubble area and illustrates the brightness of the bubble.

	??ε_r (-)	??σ(mS/m)	??ε_r (%)	??σ (%)
True anomaly	13.00	10.29	100	100
Dense	7.27	3.26	56	35
Sparse 1	7.25	4.3	56	42
Sparse 2	7.44	4.6	57	45
Sparse 3	7.48	4.15	58	40
Sparse 4	7.80	2.97	60	29
Sparse 5	6.91	3.22	53	31
ZOP	3.27	1.05	25	10

Table 2: Maximum values of true and resolved ε_r and σ anomaly magnitudes estimated for each acquisition setup. See section 3.1 and Figures 3 and 4 for details.

The permittivity model obtained from ZOP data differs significantly from the results discussed above (Fig. 3H, 3P). The gas bubble appears as a low-permittivity layer in the correct depth interval. The magnitude of the resolved anomaly is 25% of the true anomaly, and the obtained subsurface ε_r background model is smoother than those obtained using MOG acquisition (see Table 2).

Figures 4B-4G show σ models obtained using the dense MOG data and the different sparse MOG data subsets. The influence of reducing traces on the obtained σ images is clearer than for the ε_r images. For the first three sparse setups presented in Figures 4C-E and 4K-4M, the shape, location and magnitude of the gas bubble is resolved in a similar manner as when using the dense acquisition geometry (Fig. 4B, 4J). When the number of traces is reduced further, the gas bubble is slightly more difficult to outline from the background distribution (Fig. 4F-4G). Differences in the performance of the selected acquisition strategy are also seen on the magnitudes of the resolved anomalies. The dense reference setup results in a slightly smoother model than the first three sparse geometries. While the maximum recovered anomaly magnitude is 35% for the dense geometry, the Sparse Geometries 1-3 resolve 40-45% of the true magnitude (Fig. 4J-4M, Table 2). Sparse Geometries 4-5 result in a weaker anomaly than the dense reference geometry and only resolve approximately 30% of the true anomaly magnitude (Fig. 4J, 4N-3O, Table 2). In contrast to the ε_r model obtained from ZOP data, the corresponding σ model does not show the depth of the gas bubble. Essentially no change in the subsurface conductivity is seen induced by the gas bubble (Fig. 4H, 4P).

Sparse Geometry 2 with 1 m transmitter spacing and 25 cm receiver spacing results in the best ε_r and σ final models (Fig. 3D, 3L, 4D, 4L). Moreover, the estimated time for acquiring this dataset is significantly shorter compared to choosing, e.g., Sparse Geometry 1 (see Table 1). The final ε_r model obtained from Sparse Geometry 3 is also relatively well-resolved and the final σ is only slightly less well-constrained as compared to the most optimal Sparse Geometry 2(Fig. 3E, 3M, 4D-4E, 4L-4M). The dataset collected using the survey geometry of Sparse 3 may also be slightly faster to collect. The delay time during recording traces between subsequent receiver positions depends on the field conditions, for example the antenna cables may tangle easier or be more challenging to place in at the accurate vertical depth location if the receiver is moved in big steps rather than in small steps necessitating more than 3 seconds between subsequent traces.

3.2. Comparison of noise-free and noisy data

The acquisition geometry test presented in chapter 3.1 is conducted using noise-free data. In order to investigate the impact of noise on the final FWI results, we test three different scenarios. The three tests only differ in the level of random noise (see Figure 2).

The noise tests are initially carried out with the dense acquisition setup. Final ε_r models obtained from the noisy datasets (Fig. 5C-5E) show characteristics similar to the models obtained from noise-free data which is included in Fig. 5B to facilitate comparison. The depth of the gas bubble is well captured, but the shape of the bubble changes slightly when noise is introduced. In the low-noise scenario the change is not easily recognized. As the noise increases, the bubble becomes more horizontally elongated than in the noise-free scenario (Fig. 5B-5E). Also, the magnitude of the resolved ε_r anomaly is affected by the noise: The amplitude of the recovered anomaly decreases with increasing noise, and the strong negative areas directly above and below the bubble become weaker as the noise level increases (Fig. 5G-5J), see Table 3.

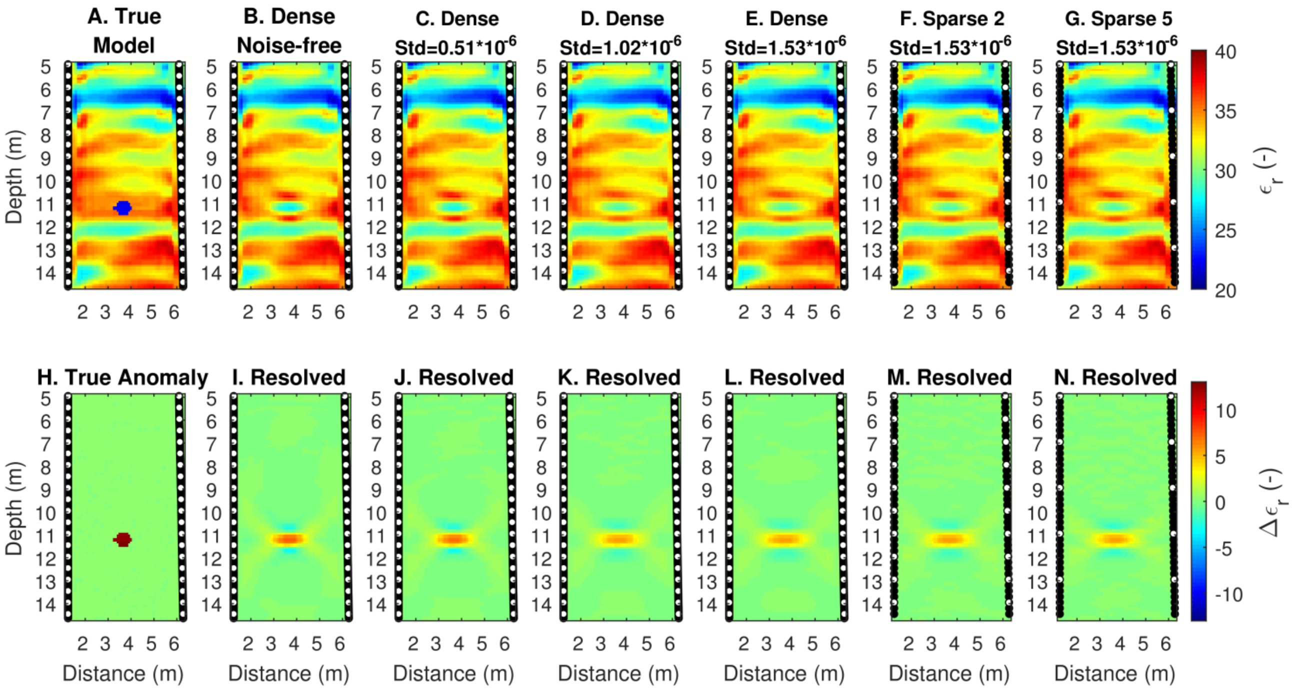

Figure 5: Panel A shows the true subsurface ε_r distribution and H shows the true anomaly magnitude. Final ε_r models obtained from noise-free data (B) and noisy data (C-G) are similar to one another. The gas bubble becomes slightly more horizontally elongated as the noise level increases (B-E). Also, the magnitude of the resolved bubble becomes weaker with increasing noise (I-L). Permittivity models obtained from highly noisy data are not greatly affected by the selected acquisition geometry (E-G). In all cases with a high noise level, the magnitude of the resolved anomaly is approximately 50% of the true magnitude.

	??ε_r (-)	??σ (mS/m)	??ε_r (%)	??σ (%)
True anomaly	13	10.29	100	100
Noise-free (Dense)	7.27	3.62	56	35
Low noise (Dense)	6.74	2.17	52	21
Medium noise (Dense)	5.55	1.72	43	17
High noise (Dense)	5.56	1.78	43	17
High noise (Sparse 2)	5.60	1.81	43	18
High noise (Sparse 5)	5.42	1.93	42	19

Table 3: True and resolved maximum anomalies using noisy data.

While the ε_r models do not change drastically from the noise-free results, σ results are significantly affected by the noise (Fig. 6). All of the noisy data scenarios show that the gas bubble is quite difficult to outline from the background ε_r model. Also the amplitude of the resolved anomaly is clearly lower than in the models obtained from noise-free data.

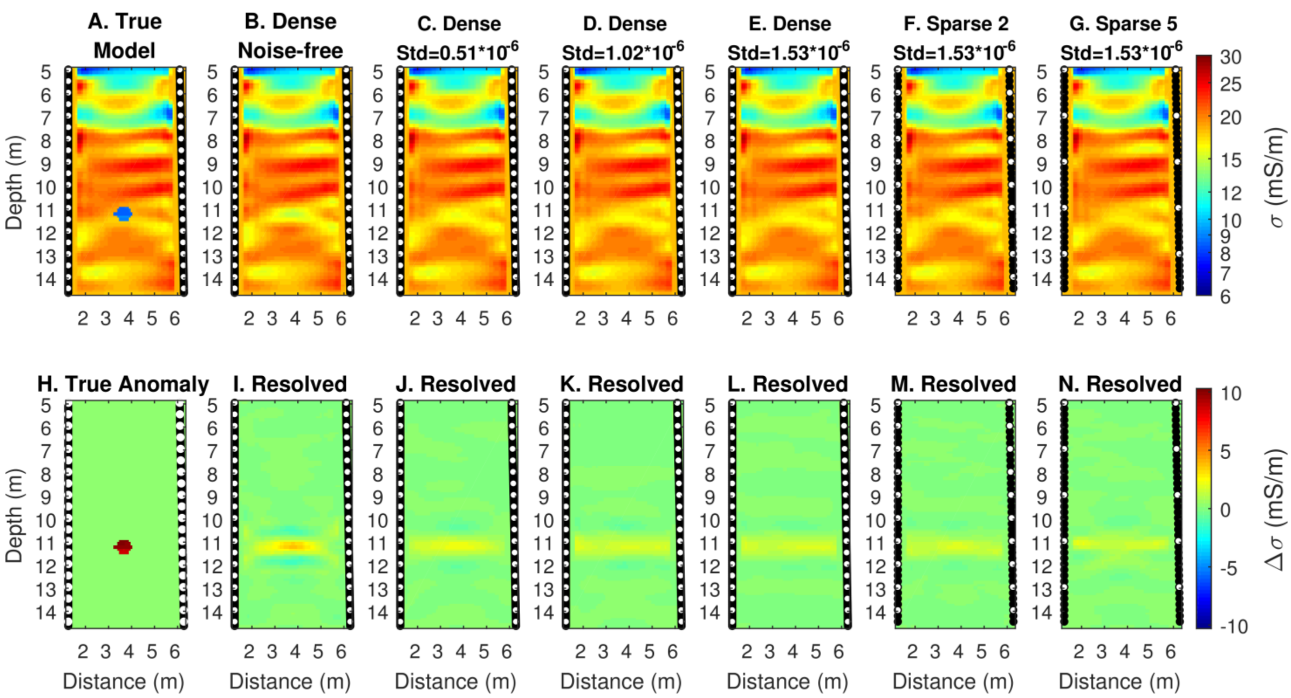

Figure 6: Panels A and H show the true subsurface σ distribution and the true anomaly magnitude, respectively. The noise-free data results in a clearly better σ model than the noisy datasets (B-G). The influence of the added noise is also seen in the resolved magnitudes (I-N).

Reducing data coverage does not have a notable influence on the final results. For comparison, we apply Sparse Geometries 2 and 5 on the high-noise data shown in Figure 2C. The ε_r and σ models show the same characteristics as the models resolved using the dense geometry (Figs. 5E-5G, 6E-6G, Table 3). Similarly to the observations from different acquisition geometries (Figs. 3-4), the gas bubble in the ε_r model becomes laterally more elongated if the dense acquisition geometry is applied than if either Sparse Geometry 2 or 5 is chosen (Fig. 5E-5G). All tested survey geometries result in rather poor σ models. The location of the gas bubble cannot be clearly observed (Fig. 6E-6G).

3.3. Increasing bubble size

In the last test, we increase the bubble size and use the high-noise data in FWI. The big gas bubble is almost three times as big as in the previous experiments. Gas saturation in the big bubble is again 30% and it produces a low-conductivity and low-permittivity anomaly in the subsurface (Figs. 7A, 7E, 8A, 8E).

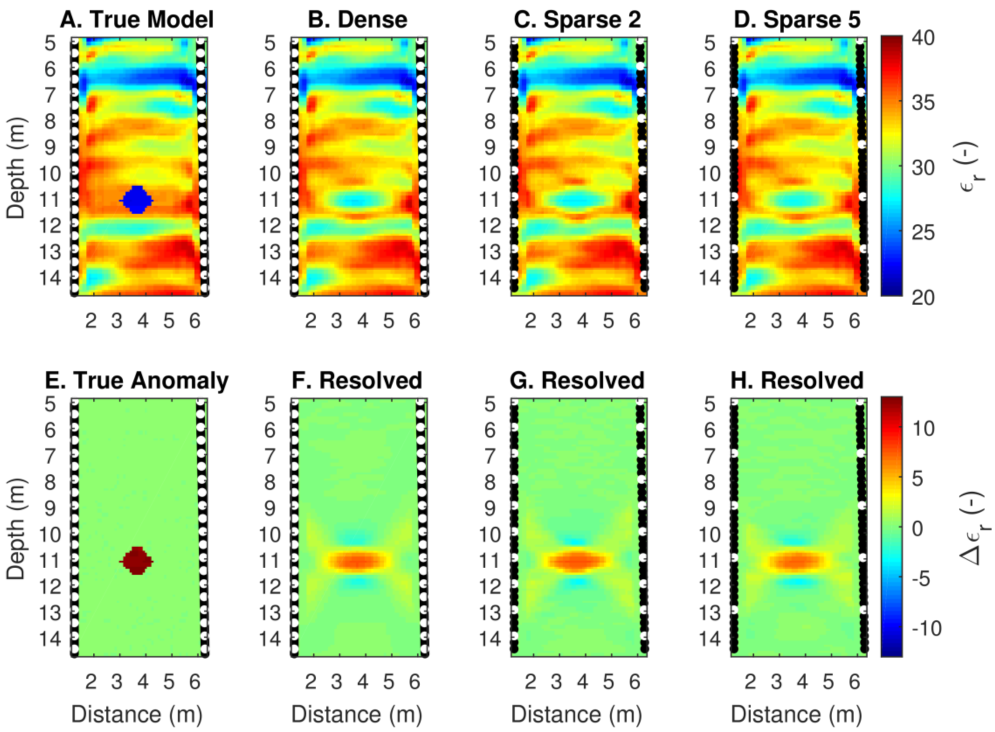

Figure 7: ε_r models obtained from highly noisy data (B-D) using Dense and Sparse Geometry 2 and 5. Corresponding resolved anomaly magnitudes are shown in F-H.

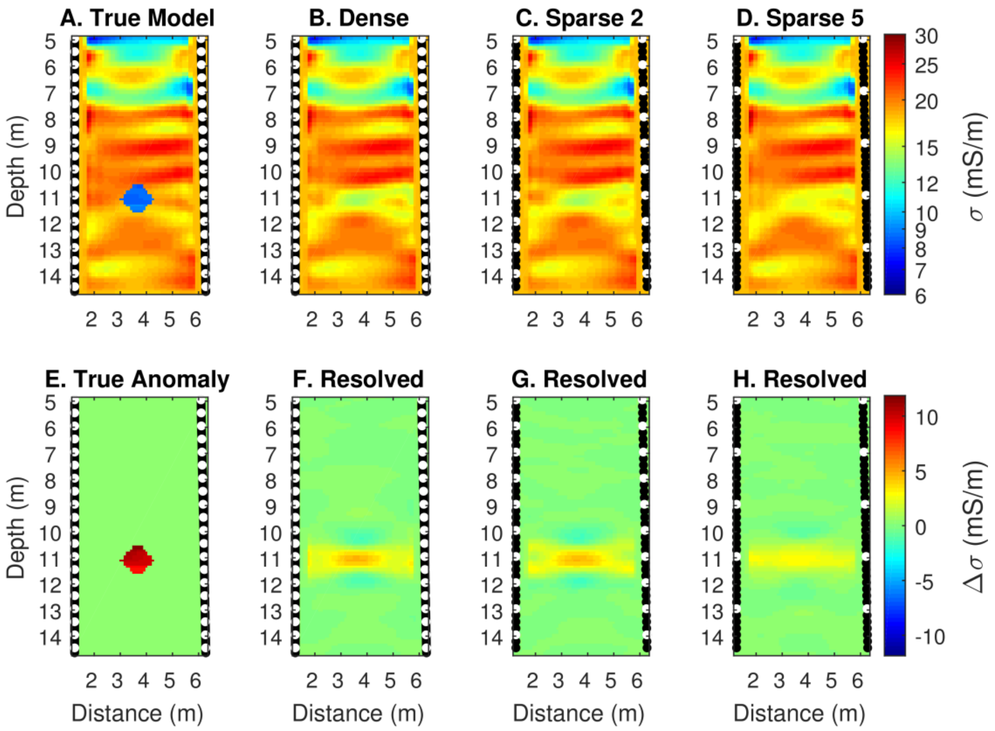

Figure 8: σ models obtained from highly noisy data (B-D) using Dense and Sparse Geometry 2 and 5. Corresponding resolved anomaly magnitudes are shown in F-H.

Dense and Sparse Geometry 2 result in better subsurface models than Sparse Geometry 5 (B-D). The resolved anomaly magnitude using the dense and the Sparse Geometry 2 is almost 40% of the true anomaly magnitude (F-G) while the Sparse Geometry 5 poorly recovers the location and the magnitude of the anomaly. The resolved ε_r models show small differences in the shape of the big gas bubble (Fig. 7B-7D). In all tested survey geometries the magnitude of the anomaly is 54-58 % of the true anomaly magnitude (Fig. 7E-7H). The areas showing high permittivity directly above and below the bubble become clearer as data coverage is reduced (Fig. 7B-7D). Increasing the size of the gas bubble improves the subsurface σ models. The dense reference geometry and the Sparse Geometry 2 now result in a clearly visible bubble (Fig. 8B-8C). The location of the injected gas is well resolved and the anomaly magnitude is 38-39% of the true subsurface anomaly (Fig. 8E-8G). As the data coverage is reduced further, the gas bubble again becomes difficult to outline from the background (Figs. 8D, 8H, Table 4). Overall, the observations from increasing the bubble size are consistent with the results obtained from noise-free data (see section 3.1).

	??ε_r (-)	??σ (mS/m)	??ε_r (%)	??σ (%)
True anomaly	13	11.86	100	100
Dense	7.57	4.65	58	39
Sparse 2	7.58	4.47	58	38
Sparse 5	7.02	2.94	54	25

Table 4: True and resolved anomaly magnitudes using a big gas bubble and noisy data. See section 3.3 for details.

3.4. Additional tests

In addition to the tests presented in 3.1-3.3, we investigate how the dense and the sparse geometry 2 resolve the subsurface models if the small gas bubble with 30% gas saturation is located in a low-permittivity zone at approximately 12 m depth. The collected crosshole GPR data in this test is noise free. In this new geological setting, the anomaly caused by the gas bubble in the ε_r models is 10 units lower than the surrounding media and is therefore regarded as a moderate anomaly. In the σ model the anomaly is approximately 14 units lower than the surrounding media and causes a strong local anomaly. The obtained results are consistent with the acquisition geometry tests shown in section 3.1 and do not therefore appear to depend on the location of the bubble, and the results are therefore not included here.

As the resolved anomaly is more difficult to outline from the σ models than from the ε models, we also test if a homogeneous conductivity starting model (σ = 17 mS/m) results in more appropriate σ models than the true background σ distribution. The conductivity starting model test is carried out with the two different geological settings where the small gas bubble with 30% gas saturation is either located in a high permittivity zone or in the low permittivity zone. The measured data is again noise-free and we apply the dense reference acquisition geometry and the sparse geometry 2. The homogeneous σ starting model results in slightly better σ models than the true background σ distribution, as the resolved anomaly induced by the gas bubble is easier to delineate and has stronger amplitude. However, resulting ε_r models become less optimal for both acquisition geometries. The resolved anomaly in the ε_r model has lower amplitude and a smaller size than in the results obtained using the true background σ distribution.

4. Discussion

FWI has proven to be a strong tool for resolving fine-grained permittivity structure and strong contrasts in important chalk reservoir rock types, which in turn may be used to estimate porosity fluctuations comparable to what can obtained from rock sample measurements (Keskinen et al., 2017). The porosity models estimated using FWI indicate low-porosity (high permittivity) areas as well as high-porosity (low permittivity) zones (Keskinen et al., 2017), which most likely play an important role for determining fluid/gas flow pathways. However, the porosity model alone does not reflect all reservoir properties as the pores may, for example, be isolated and do not necessarily contribute significantly to flow through the rock. Therefore, fluid or gas flow experiments are needed for a more complete description of the flow properties of the rock, and behaviour of e.g., CO_2 gas may be particularly important to study with time-lapse GPR experiments (e.g., Yuan et al., in press). Efficient and fast sampling of cross-hole GPR data is essential since the gas may dissolve or escape quickly, depending on the bulk permeability and the existence of fractures and faults (e.g., Lassen et al., 2015).

In this study, we have performed synthetic tests linked to resolving an injected gas bubble using different crosshole GPR transmitter-receiver geometries, which take from several hours (or more than a day) to a few hours to collect, depending on the GPR equipment available. Moreover, we have made the experiments for a realistic, highly heterogeneous chalk succession, which serves as a background model of our experiments. We consider the choice of background model essential for any such synthetic resolution test, because the permittivity (i.e. velocity) distribution of this model is highly determining for the travel paths of the wave field in the subsurface. The dense reference geometry samples the gas bubble much more densely in the horizontal than in the vertical direction (Fig. 1A). Therefore, the dense geometry leads to a slightly more elongated gas bubble than the sparser geometries tested here, as the relatively many travel paths in the horizontal or sub-horizontal direction tend to smear the anomaly. Not surprisingly, as the data coverage is reduced, lateral smearing is less visible but at the same time leads to a stronger overshooting in the anomaly estimation directly above and below the resolved gas bubble than if the dense survey geometry is used (Figs. 3B-3E, 3J-3M, 4B-4E, 4J-4M). These models are all considered acceptable for a time-lapse experiment as the location of the gas bubble and the background models are well resolved. However, if the data coverage is reduced further (Sparse Geometry 4 and 5), the background ε model is poorly resolved and the gas bubble can hardly be outlined in the σ model (Figs. 3F, 4F). While the MOG geometries are capable of sampling the gas bubble both horizontally and vertically, ZOP geometry can only sample it horizontally, depending on the exact permittivity (velocity) structure. In this case, the bubble appears as a layer in the ε_r model and only indicates the depth interval of the injected gas (Fig. 3H, 3P). Following a simple ZOP strategy is fast and may thus be sufficient if only mapping of the upper and lower layer boundaries of where gas occurs is the target of the cross-hole investigation.

The noise test conducted with the dense reference geometry indicates that lateral smearing increases with increasing random noise and over-estimation of the dielectric permittivity directly above and below the gas bubble decreases. Also the magnitude of the resolved anomaly decreases with increasing noise (Figs. 5B-5E, 5I-5L). Thus, the noisy data is less well fitted by the FWI algorithm than the noise-free data, and the resulting subsurface models have a smoother appearance. Similar to the noise-free scenarios, reducing the data coverage in the case where noise is present reduces the lateral smearing effect and local overestimation of the dielectric permittivity again becomes stronger than for the reference geometry (Figs. 5F-5G, 5M-5N). In general, the estimation of the conductivity structure is more affected by the presence of random noise than the estimation of the permittivity structure.

Different effects of uncorrelated, random noise as well as correlated data errors have been investigated in previous studies (e.g., Cordua et al., 2008). Moreover, the dominant noise in GPR cross-hole data sets may not be uncorrelated. Correlated data errors caused by e.g. misplacement of the antennae or unknown borehole irregularities may have a larger effect than typical uncorrelated, random noise (Cordua et al., 2008), and such error types cannot be effectively suppressed simply by changing source-receiver geometries and the data density. However, detailed studies of the influence of noise are not the main focus points of this study. Instead, we refer the reader to other studies (e.g., Cordua et al., 2008) based on which the influence of different expected noise types can be assessed.

Conductivity models resolved using the noisy datasets are not very useful regardless of the chosen survey geometry. The small gas bubble is clearly below the resolution of the obtained σ models in all cases (see Fig. 6). When the size of the gas bubble is increased significantly, the Sparse Geometry 2 results in acceptable ε_r and σ models. Reducing the data coverage further again results in a rather poor σ model (Figs. 7-10). Conductivity models seem to have significantly higher sensitivity to the noise and to the data coverage than permittivity models. These observations are consistent with the results by e.g., Oberröhrmann et al. (2013) who found that σ models have a lower resolution than ε_r models. Permittivity of a medium is mainly affected by the shape of the measured data, while the electrical conductivity is strongly influenced by the amplitude. Small changes at the amplitude of the data such as caused by noise interference can therefore have a significant effect on the FWI conductivity results. Better resolved conductivity and permittivity models can be obtained by increasing the bubble size (see Tables 3 and 4). Also, a resolved conductivity change closer to the true anomaly is obtained when using a homogeneous conductivity starting model in the FWI. However, this is at the expense of the resolved permittivity magnitude and structure.

Evidently, we have only considered the (simple) two-dimensional (2D) case in our synthetic tests of gas bubble simulation. Clearly, 3D effects (out of plane) will occur under real conditions, although the chalk deposits are expected to be fairly uniformly layered over relatively short intervals as studied here (e.g., Surlyk et al., 2006; Keskinen, 2017). In particular, unknown, possible small fractures may add to 3D effects under real conditions.

Overall, our findings seem to be consistent with the survey design studies performed by Maurer et al. 2010, which included cross-hole seismic tomographic elements, although our study is based on GPR and linked to a specific field site where the sub-surface consists of a heterogeneous chalk-rich rock.

5. Conclusions

In this study, we conducted a synthetic test in order to optimize the information content of a time-lapse crosshole GPR data survey while minimizing the number of data to be collected and thereby reducing acquisition time. The synthetic test was based on a published field data study in chalk and therefore includes a strongly heterogeneous, realistic dielectric permittivity distribution.

Seven different survey geometries were tested with varying amounts of collected traces (from 6240 to 78) and, therefore, also strongly varying acquisition times (from ~512 min to ~14 min).

For the noise-free test, the amount of traces required to resolve a gas bubble could be reduced substantially (from 6270 to 375) with almost no adverse effect on the resulting permittivity structure, given that a dense background survey was collected before gas injection. As expected, introducing a high noise level affected the recovery of the permittivity magnitude of the anomaly using the dense survey geometry (from 56% to 43% of the true anomaly value), but the magnitude was not markedly deteriorated by reducing the amount of collected traces (a reduction of 1% and 4% for the small and large anomaly test, respectively). The effect of noise on the resulting electrical conductivity distribution was, on the other hand, significantly stronger for the large anomaly test (a reduction of the anomaly value from 39% to 25% of the true anomaly value). Similar to previously published work, we found the conductivity distribution to be more challenging to resolve than the permittivity distribution.

The results presented in this paper may serve as a catalogue of survey geometries to choose from, depending on the resolution needed and practical possibilities related to data acquisition speed and recording systems available for crosshole GPR experiments. In this context, the expected level of uncorrelated, random noise as well as possible sources of correlated data errors should be taken into account.

We find it particularly interesting that even rather sparse geometries, which can be recorded during little over an hour, can in fact pinpoint the position of a relatively small gas bubble with an acceptable degree of resolution, thereby, making cross-hole GPR data a feasible method to visualize tracer movement during time-lapse experiments. Special care needs to taken if a tracer is chosen that mainly influences the electrical conductivity results (e.g., salt tracer). In such a case the acquisition geometry needs to be adapted to still retrieve quantitative results.

Acknowledgements

We gratefully acknowledge Maersk Oil for financing this study. We also thank Hansruedi Maurer (ETH Zürich) for his excellent comments for improving the paper. We thank reviewer and associate editor for their comments to an earlier version of this manuscript.

References

Binley, A., P. Winship, R. Middleton, M. Pokar, and J. West, 2001. High-resolution characterization of vadose zone dynamics using cross-borehole radar. Water Resources Research 37 (11), 2639–2652, Doi: 10.1029/2000WR000089

Cahill, A.G. and R. Jakobsen, 2013. Hydro-geochemical impact of CO2 leakage from geological storage on shallow potable aquifers: A field scale pilot experiment. International Journal of Greenhouse Gas Control 19, 678-688, Doi: 10.1016/j.ijggc.2013.03.015

Cordua, K.S., M.C. Looms and L. Nielsen, 2008. Accounting for correlated data errors during inversion of cross-borehole ground penetrating radar data. Vadose Zone Journal 7, 263-271

Davis, J.L., and A.P. Annan, 1989. Ground-penetrating radar for high-resolution mapping of soil and rock stratigraphy. Geophysical Prospecting, 37 (5), 531-551, Doi: 10.1111/j.1365-2478.1989.tb02221.x

Day-Lewis, F. D., J. W. Lane, Jr., J. M. Harris, and S. M. Gorelick, 2003. Time-lapse imaging of saline-tracer transport in fractured rock using difference-attenuation radar tomography. Water Resources Research, 39(10), 1290, Doi:10.1029/2002WR001722

Ernst, J.R., H. Maurer, A.G. Green, and K. Holliger, 2007a. Full-Waveform Inversion of Crosshole Radar Data Based on 2-D Finite-Difference Time-Domain Solutions of Maxwell ’ s Equations. IEEE Transactions in Geoscience and Remote Sensing 45 (9), 2807–2828, Doi: 10.1109/TGRS.2007.901048

Ernst, J.R., A.G. Green, H. Maurer, and K. Holliger, 2007b. Application of a new 2D time-domain full-waveform inversion scheme to crosshole radar data. Geophysics 72 (5), J53–J64, Doi:10.1190/1.2761848

Gueting, N., A. Klotzsche, J. van der Kruk, J. Vanderborght, H. Vereecken, and A. Englert, 2015. Imaging and characterization of facies heterogeneity in an alluvial aquifer using GPR full-waveform inversion and cone penetration tests. Journal of Hydrology 524, 680-695, Doi: 10.1016/j.hydrol.2015.03.030

Haarder E. B., A. Binley, M. C. Looms, J. Doetsch, L. Nielsen, and K. H. Jensen, 2012. Comparing Plume Characteristics Inferred from Cross-Borehole Geophysical Data. Vadose Zone Journal 11(4), Doi: 10.2136/vzj2012.0031

Hubbard, S. S., J. E. Peterson, Jr, E. L. Majer, P. T. Zawislanski, K. H. Williams, J. Roberts, and Frank Wobber, 1997. Estimation of permeable pathways and water content using tomographic radar data. The Leading Edge 16(11), 1623-1630. Doi: 10.1190/1.1437539

Irving, J.D., and R.J. Knight, 2005. Effect of antennas on velocity estimates obtained from crosshole GPR data. Geophysics 70 (5), K39–K42, Doi:10.1190/1.2049349

Keskinen, J., A. Klotzsche, M. C. Looms, J. Moreau, J. van der Kruk, K. Holliger, L. Stemmerik, and L. Nielsen, 2017. Full-waveform inversion of crosshole GPR data: Implications for porosity estimation in chalk. Journal of Applied Geophysics 140, 102–116, Doi: 10.1016/j.jappgeo.2017.01.001

Klotzsche, A., J. van der Kruk, G.A. Meles, J. Doetsch, H. Maurer, H., and N. Linde, 2010. Full-waveform inversion of cross-hole ground-penetrating radar data to characterize a gravel aquifer close to the Thur River, Switzerland. Near Surface Geophysics 8 (6), 635–649, Doi:10.3997/1873-0604.2010054

Klotzsche, A., J. van der Kruk, J. Bradford, and H. Vereecken, 2014. Detection of spatially limited high-porosity layers using crosshole GPR signal analysis and full-waveform inversion. Water Resources Research 50 (8), 6966–6985, Doi: 10.1002/2013WR015177

Klotzsche, A., J. van der Kruk, N. Linde, J. Doetsch, and H. Vereecken, 2013. 3-D characterization of high-permeability zones in a gravel aquifer using 2-D crosshole GPR full-waveform inversion and waveguide detection. Geophysical Journal International 195 (2), 932-944.

Klotzsche, A., F. Jonard, M.C. Looms, J. van der Kruk, and J.A. Huisman, 2018. Measuring soil water content with ground penetrating radar: a decade of progress. Vadose Zone Journal 17. http://doi.org/10.2136/vzj2018.03.0052.

Klotzsche, A., H. Vereecken, and J. van der Kruk, 2019. Review of Crosshole GPR Full-waveform Inversion of Experimental Data: Recent Developments, Challenges and Pitfalls. Geophysics, in press.

Lassen, R.N., T.O. Sonnenborg, K.H. Jensen, and M.C. Looms, 2015. Monitoring CO2 gas-phase migration in a shallow sand aquifer using cross-borehole ground penetrating radar. International Journal of Greenhouse Gas Control 37, 287–298, Doi: 10.1016/j.ijggc.2015.03.030

Lesmes, D.P., and S.P. Friedman, 2005. Relationships between the electrical and hydrogeological properties of rocks and soils. in: R. Yoran and S.S. Hubbard, eds, Hydrogeophysics, Springer, Water Science and Technology Library No. 50, 87–128, Doi: 10.1007/1-4020-3102-5_4

Lebron, I., D.A. Robinson, S. Goldberg, and S.M. Lesch, 2004. The Dielectric Permittivity of Calcite and Arid Zone Soils with Carbonate Minerals. Soil Science Society of America Journal 68 (5), 1549–1559, Doi: 10.2136/sssaj2004.1549

Looms, M.C., K.H. Jensen, A. Binley, and L. Nielsen, 2008. Monitoring unsaturated flow and transport using geophysical methods. Vadose Zone Journal 7 (1), 227-237, Doi:10.2136/vzj2006.0129

Maurer, H., Curtis, A., Boerner, D.E., 2010. Recent advances in optimized geophysical survey design. Geophysics 75, doi: 10.1190/1.3484194.

Meles, G.A., J. van der Kruk, S.A. Greenhalgh, J.R. Ernst, and H. Maurer, A.G. Green, 2010. A new vector waveform inversion algorithm for simultaneous updating of conductivity and permittivity parameters from combination crosshole/borehole-to- surface GPR data. IEEE Transactions on Geoscience and Remote Sensing 48 (9), 3391–3407, Doi: 10.1109/TGRS.2010.2046670

Mount, G. J., and X. Comas (2014). Estimating porosity and solid dielectric permittivity in the Miami Limestone using high-frequency ground penetrating radar (GPR) measurements at the laboratory scale. Water Resources Research 50, 7590–7605, Doi: 10.1002/2013WR014947

Oberröhrmann, M., A. Klotzsche, H. Vereecken, and J. van der Kruk, 2013. Optimization of acquisition setup for cross-hole GPR full-waveform inversion using checkerboard analysis. Near Surface Geophysics 11 (2), 197–209, Doi: 10.3997/1873-0604.2012045

Peterson, J. E. Jr., 2001. Pre-inversion Corrections and Analysis of radar Tomographic Data. Journal of Environmental and Engineering Geophysics 6 (1), 1-18, Doi: 10.4133/JEEG6.1.1

Surlyk, F., Damholt, T., Bjerager, M., 2006. Stevns Klint, Denmark: uppermost Maastrichtian chalk, Cretaceous-Tertiary boundary, and lower Danian bryozoan mound complex. Bull. Geol. Soc. Den. 54, 1–48.

Tomlinson D.W., N.R. Thomson, R.L. Johnson, J.D. Redman, 2003. Air distribution in the Borden aquifer during in situ air sparging, Journal of Contaminant Hydrology. 67 (1–4), 113-132,Doi: 10.1016/S0169-7722(03)00070-6

Witthüser, K., H. Hötzl, B. Reichert, W. Stichler, and R. Nativ, 2000. in A. Dassargues (eds.) Tracers and Modelling in Hydrogeology (Proceedings of the TraM'2000 Conference held at Liège, Belgium, May 2000), IAHS Publication No. 262, ISBN: 1-901502-21-X

Yang, X., A. Klotzsche, G. Meles, H. Vereecken, J. van der Kruk, 2013. Improvements in crosshole GPR full-waveform inversion and application on data measured at the Boise Hydrogeophysics Research Site. Journal of Applied Geophysics 99, 114–124, Doi: 10.1016/j.jappgeo.2013.08.007

Yuan, H., M.C. Looms and L. Nielsen, in press. On the usage of diffractions in GPR reflection data – implications for time-lapse gas migration monitoring. Geophysics, Doi: 10.1190/geo2019-0343.1

List of Tables

List of Figure captions

Figure 1: Data coverage for the first half of each dataset transmitter positions are indicated with red circles and receiver positions with blue dots. Table 1 shows the data acquisition parameters for each of the survey geometry.

Figure 2: (A) Low, (B) intermediate, and (C) high noise added on the synthetic data (red). The noise is random Gaussian noise with a standard deviation *std* of, $0.51 \cdot 10^{-6}$, $1.02 \cdot 10^{-6}$, and $1.53 \cdot 10^{-6}$, respectively. The black trace represents the noise free trace.

Figure 3: The true subsurface ε_r model (A) and the resolved ε_r models obtained from the different acquisition geometries (B-H). True anomaly magnitude (I) is obtained by subtracting the true subsurface ε_r model from the ε_r starting model. The resolved anomaly magnitudes (J-P) are estimated by subtracting the final ε_r model from the ε_r starting model. Transmitter and receiver positions are indicted with circles and crosses, respectively.

Figure 4: The true subsurface σ model (A) and the resolved σ models obtained from the different acquisition geometries (B-H). True anomaly magnitude (I) is obtained by subtracting the true subsurface σ model from the σ starting model. The resolved anomaly magnitudes (J-P) are estimated by subtracting the final σ model from the σ starting model.

Figure 5: Panel A shows the true subsurface ε_r distribution and H shows the true anomaly magnitude. Final ε_r models obtained from noise-free data (B) and noisy data (C-G) are similar to one another. The gas bubble becomes slightly more horizontally elongated as the noise level increases (B-E). Also, the magnitude of the resolved bubble becomes weaker with increasing noise (I-L). Permittivity models obtained from highly noisy data are not greatly affected by the selected acquisition geometry (E-G). In all cases with a high noise level, the magnitude of the resolved anomaly is approximately 50% of the true magnitude.

Figure 6: Panels A and H show the true subsurface σ distribution and the true anomaly magnitude, respectively. The noise-free data results in a clearly better σ model than the noisy datasets (B-G). The influence of the added noise is also seen in the resolved magnitudes (I-N).

Figure 7: ε_r models obtained from highly noisy data (B-D) using Dense and Sparse Geometry 2 and 5. Corresponding resolved anomaly magnitudes are shown in F-H.

Figure 8: σ models obtained from highly noisy data (B-D) using Dense and Sparse Geometry 2 and 5. Corresponding resolved anomaly magnitudes are shown in F-H.